ENGINEERING

Multiscale analysis of equatorial sclera anisotropy: Revealing discrepancies in fiber orientation and mechanical properties

Runze Li[1,2]†‡, Yi Hua[3,4,5]†, Fengyi Zhang[6,7]†, Xuejun Qian[1,2], Chen Gong[2], Xiao Wan[8], Susannah Waxman[3], Yushun Zeng[1], Ziyuan Che[8]§, Junhang Zhang[2], Wei Jin[6,7], Mark S. Humayun[1,2,9], Zhongping Chen[6,7]*, Ian A. Sigal[3,4]*, Qifa Zhou[1,2,9]*

The sclera, the eye's primary load-bearing tissue, substantially influences the globe's response to intraocular pressure. Although the mechanical properties of the anterior and posterior segments have been extensively studied, the equatorial sclera's properties remain underexplored, limiting our understanding of ocular conditions like myopia, ocular trauma, and glaucoma. Traditional studies that rely solely on fiber orientation to explain scleral mechanics may overlook the tissue's complex biomechanical behavior. To address this gap, we conducted a comprehensive investigation using ultrasonic elastography, optical coherence elastography, and polarizing light microscopy to analyze the equatorial sclera's anisotropic properties. Our findings reveal a counterintuitive result: Mechanical anisotropy in the equatorial sclera contradicts preferred fiber orientation. This integrated approach not only challenges prevailing models of scleral biomechanics but also provides fundamental insights into the mechanisms underlying key ocular conditions, highlighting the importance of multimodal and multiscale analyses in biological tissue research.

INTRODUCTION

The eye is composed of several anisotropic tissues, cornea (*1*), iris (*2*), ciliary body (*3*), lens (*4*), retina (*5*), and sclera (*6*), whose directional mechanical properties are integral to their specific physiological functions. Among these, the sclera, a resilient fibrous tissue extending from the cornea in the front, to the optic nerve head (ONH) in the back, serves as the eye's primary shield against external damage while concurrently withstanding internal fluctuations in intraocular pressure (IOP) (*7*). The biomechanical role of the sclera, particularly in the posterior region and around the ONH, has attracted considerable interest due to its association with susceptibility to glaucoma. The anisotropy of the posterior sclera, understood to influence biomechanical changes during glaucoma progression, reinforces circumferential mechanical properties and curtails scleral canal expansion (*8*–*11*). However, the biomechanics of the equatorial sclera remain critically understudied, despite its relevance in protecting the retina from mechanical strain (*12*). A detailed understanding of biomechanical changes during IOP elevation or disease progression is essential not only for glaucoma but also for other vision-threatening disorders such as myopia.

Myopia is a common ocular disorder caused by a mismatch between the optical path and axial length; distant objects are imaged beyond the plane of the retina, resulting in reduced visual acuity (*13*). Global estimates highlight that nearly 1 billion individuals grapple with myopia, particularly in developed regions (*14*, *15*). A hallmark clinical feature of myopia is the axial elongation of the ocular globe. Some studies suggest that changes in the biomechanics of the sclera might contribute to this eye shape alteration in myopia (*16*). Given that myopic eyes tend to have thinner and more flexible sclera in the posterior pole (*17*), it is plausible that the biomechanical properties of the equatorial sclera are also involved in the progression of myopic deformation (*14*).

Ocular trauma further underscores the importance of understanding the biomechanics of the equatorial sclera. In the United States, eye injuries account for ~3% of emergency visits (*18*). Prompt intervention is critical, particularly in cases involving a sudden drop in IOP or risk of retinal detachment (*19*). Although traditional suturing remains the standard of care, it is time-consuming, motivating the development of faster alternatives such as thermoresponsive sealants (*20*). These sealants are designed to simplify the clinical workflow and reduce closure time during surgical repair. When trauma involves the equatorial sclera, understanding of its anisotropic mechanical properties is essential for informing the design and application of these materials, ultimately improving their mechanical integration and therapeutic performance.

A variety of tools and techniques have been developed to investigate scleral biomechanics. Although computational simulations offer valuable insights into its behavior under different stress conditions (*21*), experimental methods include tensile testing (*22*), atomic force microscopy (*23*), magnetic resonance imaging (MRI) (*24*), and notably, elastography (*25*), have been used to directly characterize its biomechanical properties. Wave-based elastography enables the induction and tracking of elastic wave propagation, which can be quantitatively

[1]Alfred E. Mann Department of Biomedical Engineering, University of Southern California, Los Angeles, CA 90089, USA. [2]Roski Eye Institute, Department of Ophthalmology, University of Southern California, Los Angeles, CA 90033, USA. [3]Department of Ophthalmology, University of Pittsburgh, Pittsburgh, PA 15219, USA. [4]Department of Bioengineering, University of Pittsburgh, Pittsburgh, PA 15213, USA. [5]Department of Biomedical Engineering, University of Mississippi, University, MS 38677, USA. [6]Beckman Laser Institute, University of California, Irvine, Irvine, CA 92612, USA. [7]Department of Biomedical Engineering, University of California, Irvine, Irvine, CA 92612, USA. [8]Department of Bioengineering, University of California, Los Angeles, Los Angeles, CA 90095, USA. [9]Allen and Charlotte Ginsburg Institute for Biomedical Therapeutics, University of Southern California, Los Angeles, CA 90089, USA.
*Corresponding author. Email: z2chen@uci.edu (Zh.C.); ian.sigal@gmail.com (I.A.S.); qifazhou@usc.edu (Q.Z.)
†These authors contributed equally to this work.
‡Present address: Department of Mechanical Engineering, Massachusetts Institute of Technology, Cambridge, MA 02139, USA.
§Present Address: Department of Chemistry and Chemical Biology, Harvard University, Cambridge, MA 02138, USA.

correlated with the mechanical properties of biological tissues (*26*). This technique is especially advantageous for its ability to noninvasively assess biomechanical changes in the sclera under varying IOP conditions, offering significant promise for in vivo and clinical applications. Within this domain, ultrasonic elastography (UE) and optical coherence elastography (OCE) are widely used in ocular studies due to their suitability for resolving the fine structures of ocular tissues (*27*–*32*).

Elastography offers direct mesoscale biomechanical insights into biological tissues, but its findings can be further contextualized and interpreted through complementary micro- to nanoscale imaging methods such as polarized light microscopy (PLM), scanning electron microscopy (SEM), and transmission electron microscopy (TEM), which allow for detailed analysis of fiber orientation and ultrastructural features. In the sclera, collagen fibers are the primary load-bearing components, and their orientation and waviness are believed to significantly influence both mechanical and anisotropic properties, due to their greater tensile strength compared to the surrounding interfibrillar matrix (*33*–*35*). Mechanical anisotropic properties of the equatorial sclera, characterized by lower stiffness in the meridional direction, have been observed in human eyes through mechanical testing (*36*). A similar anisotropic behavior has also been measured using UE and OCE by our group, with initial results previously reported (*37*–*39*), as well as by others (*40*). However, in contrast, structural analyses show that collagen fibers in this region are predominantly aligned in the meridional direction—both in pig eyes, as demonstrated by our group using PLM with preliminary findings reported earlier (*41*), and in rat eyes using small-angle light scattering (*42*). However, the dependence of equatorial scleral anisotropy on IOP, as well as its correlation with underlying microstructure and a unified mechanistic interpretation, remains poorly understood. Addressing these gaps is essential for advancing our understanding of ocular diseases such as glaucoma, myopia, and ocular trauma, where anisotropic biomechanics may significantly influence disease progression, diagnosis, and treatment strategies.

In this study, we used both UE and OCE to thoroughly investigate the biomechanical and anisotropic properties of the equatorial sclera. The complementary strengths of these techniques, with OCE providing high spatial resolution and UE offering a broad field of view (FOV), enabled both detailed regional analysis and quadrant-wide mechanical assessment (*43*–*45*). We characterized the equatorial sclera across four quadrants (nasal, superior, temporal, and inferior), two orthogonal directions (equatorial and meridional), and multiple IOP levels ranging from 10 to 30 mmHg in 5-mmHg increments. To assess the underlying microstructure, we used PLM to quantify collagen fiber orientation, supported by high-resolution ultrastructural imaging from SEM and TEM. This multimodal and multiscale approach allowed us to evaluate how scleral anisotropy depends on IOP and correlates with tissue microarchitecture. These findings improve our understanding of equatorial scleral mechanics and address important clinical concerns. More broadly, this integrated strategy offers a useful framework for characterizing the mechanical behavior of complex biological tissues.

RESULTS

Imaging systems design

Elastography systems fundamentally consist of an excitation component, responsible for instigating elastic wave propagation, and a detection component tasked with capturing these waves (see the Supplementary Materials). The measurement directions in porcine eyes used in this study were defined as shown in fig. S1. The lateral and axial resolutions of the ultrasound imaging system were measured to be 90 and 110 μm, respectively (fig. S2). For the optical coherence tomography (OCT) system, the lateral and axial spatial resolutions in air were 15.3 and 2.4 μm, respectively (Supplementary Note 2). The UE system provided a lateral FOV of 12.8 mm, sufficient to cover an entire quadrant of the equatorial sclera (fig. S3), whereas the OCE system had a lateral FOV of 3 mm, enabling only regional imaging of the equatorial sclera. In the UE setup, elastic waves were induced by a mechanical shaker, and the resulting radio frequency (rf) data were acquired using the ultrasound research platform (Vantage 256, Verasonics, Kirkland, WA, USA) as illustrated in Fig. 1A. These data were transmitted to the host PC, converted into in-phase and quadrature (IQ) data, and stored for offline analysis. A one-dimensional (1D) autocorrelation algorithm was applied to the IQ data to reconstruct a 3D matrix of axial displacement. From this matrix, spatial-temporal maps were extracted to visualize wave propagation at various depths (Fig. 1B). The elastic wave speed was calculated from the slope of the wavefront in the spatial-temporal map. A more detailed visualization of a spatial-temporal map is shown in fig. S4. To generate elastic wave speed mappings, an additional 1D autocorrelation was performed between displacement profiles at neighboring lateral positions at the same depth (fig. S5). The synchronization procedure for the UE system is detailed in fig. S6. During each measurement, the imaging target was excited with a single pulse for 1 ms, and the imaging array captured data across all lateral and depth positions, resulting in up to 200 frames per measurement session.

The OCE system uses an ultrasonic transducer for wave generation and a Doppler OCT system for wave detection (Fig. 1C). The OCT scanning beam passes through the central aperture of the ring transducer and interacts confocally with the ultrasound field, enabling both beams to converge within the same imaging plane at the target tissue at the beginning of the experiment. The transducer remains stationary while the OCT beam scans across each lateral position. At each lateral position, the transducer delivers a modulated excitation push for 2 ms, whereas the OCT system records an M-B mode image capturing both depth and time information (fig. S7). These sequential measurements are compiled into a 3D phase dataset. Spatial-temporal maps are then generated by reslicing this dataset along the depth axis, from which the elastic wave speed is calculated. For volumetric (4D) imaging, the sample was translated azimuthally with a 10-μm step size using a translation motorized linear stage (SGSP33-200, OptoSigma Corporation, Santa Ana, CA, USA) over 300 positions.

PLM leverages the birefringence of collagen fibers to determine their orientation (*46*, *47*). Although light passes through the polarizer and a birefringent material, the light intensity changes with the orientations of the sample and filter, thus providing the collagen fiber distribution and orientation (Fig. 1D). We have previously demonstrated that fixation, cryopreparation, and sectioning do not significantly alter tissue dimensions or geometry at the scales relevant to this study (*48*). Serial sections of the sclera, spanning from the exterior to the interior surface, were collected and imaged. These images were registered using fiducial markers applied prior to sectioning, allowing for reconstruction of a 3D volume. Fiber orientations were then recalculated to ensure that all in-plane measurements were accurately aligned and comparable across sections (*49*, *50*).

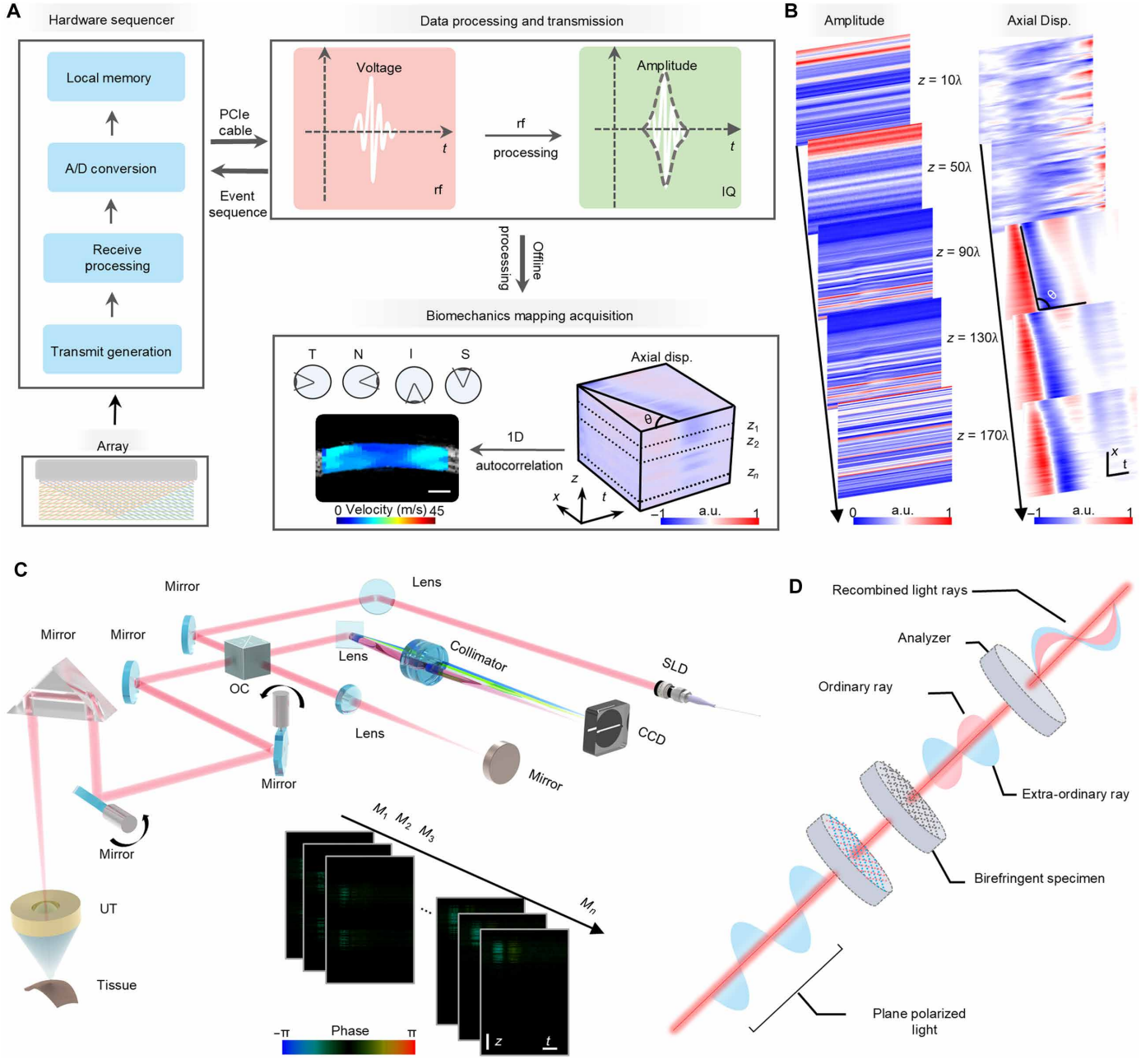

Fig. 1. System setup of UE, OCE, and PLM. (**A**) Workflow of UE. rf data were acquired, transmitted, and processed into IQ data using the hardware sequencer and host PC. During offline processing, 3D axial displacement data—comprising depth (*z*), lateral position (*x*), and time (*t*)—were reconstructed (dimension: 20 mm by 12.8 mm by 14 ms). Spatial-temporal maps at various depths were generated, where the slope angle (θ) represented the elastic wave speed in the target. The color map indicates normalized axial displacement. Final elastic wave maps were reconstructed using a 1D autocorrelation algorithm across four quadrants: temporal (T), nasal (N), inferior (I), and superior (S). Scale bar, 2 mm. (**B**) Input IQ data and reconstructed axial displacement profiles at different depths. a.u., arbitrary units. (**C**) Schematic of the OCE system. At each lateral position, M-mode images were acquired by measuring phase shifts using Doppler OCT. These M-mode images were then used to reconstruct 3D axial displacement data. Scale bars, 50 μm (*z*) and 500 μs (*t*). UT, ultrasonic transducer; OC, optical coupler; CCD, charge-coupled device; SLD, superluminescent diode. (**D**) Schematic of the PLM setup.

System accuracy validation

To assess the accuracy of the UE and OCE systems, a uniform tissue-mimicking phantom was tested with both modalities, and the results were compared (Fig. 2A). In a homogeneous, isotropic medium, elastic waves are expected to propagate the same distance in any direction over an equal time interval (Fig. 2D), and the measured propagation speed should be consistent across repeated trials. Elastic wave propagation maps generated by UE and OCE showed closely matched wave speeds (Fig. 2, F and I), and the spatial-temporal maps further confirmed system reliability (fig. S8). The measured elastic wave speeds were 2.48 ± 0.04 m/s for UE and 2.58 ± 0.03 m/s for OCE. To further confirm the UE and OCE systems' ability in discerning anisotropic

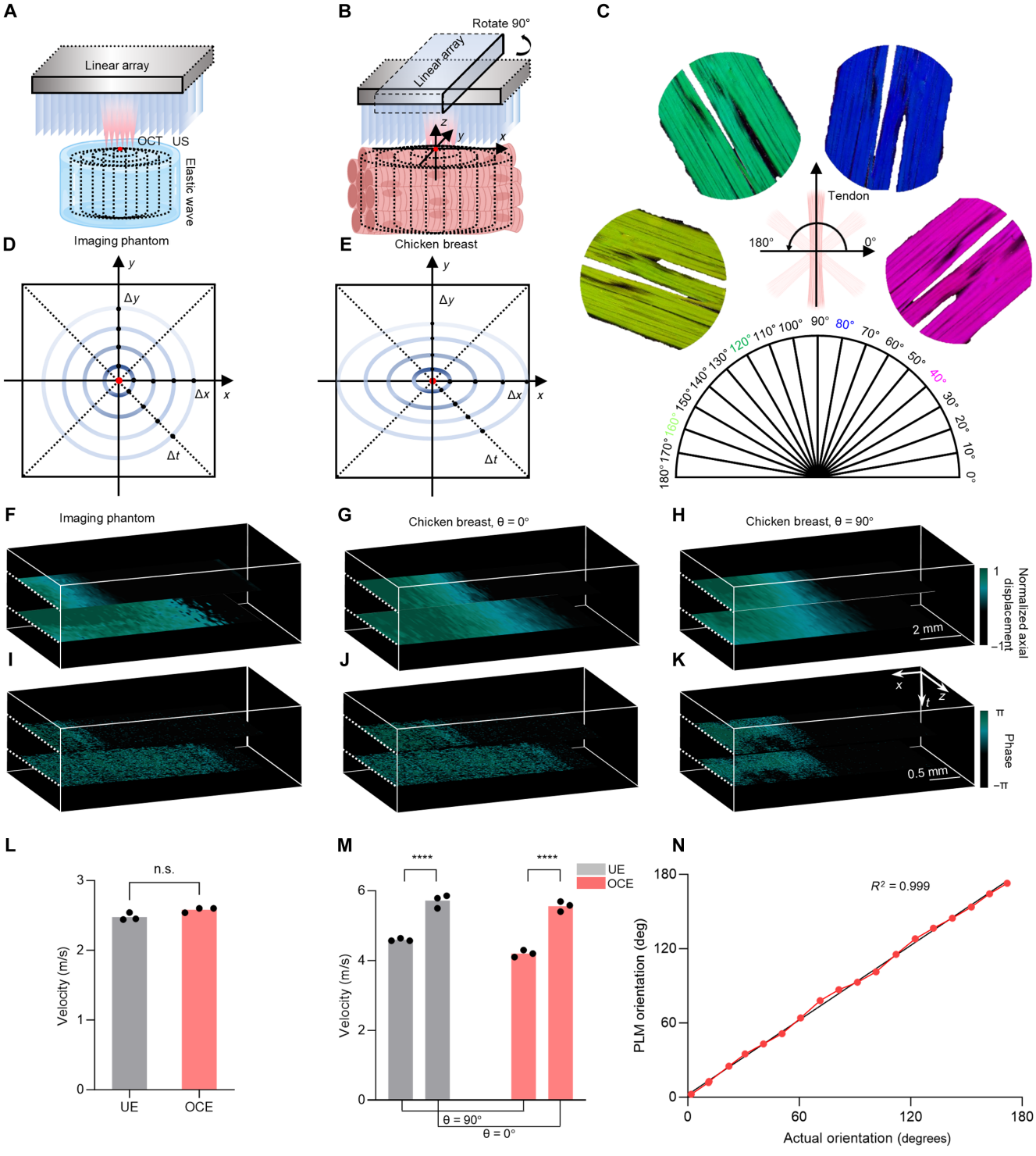

Fig. 2. Validation of UE, OCE, and PLM systems. (**A**) Accuracy test: UE and OCE measure wave speed in the same isotropic and homogeneous gelatin phantom. (**B**) Anisotropy test: Both modalities probe chicken breast with the scanning axis parallel ($\theta = 0°$) or perpendicular ($\theta = 90°$) to muscle-fiber alignment. (**C**) PLM calibration: A sheep tendon is imaged every 10° while rotated 0° to 180° to compare measured and true fiber angles. (**D**) Top-view schematic of wavefronts in the same imaging phantom: equal travel distances ($\Delta x = \Delta y$) for a fixed time Δt. (**E**) Top-view schematic of wavefronts in anisotropic chicken breast: farther propagation along fibers ($\Delta x > \Delta y$). (**F** to **H**) UE results: induced elastic wave propagation in the phantom (F), chicken breast at $\theta = 0°$ (G) and $\theta = 90°$ (H). (**I** to **K**) OCE results: elastic wave propagation in the phantom (I) and chicken breast at $\theta = 0°$ (J) and $\theta = 90°$ (K). (**L**) Elastic wave speeds in the imaging phantom measured by UE and OCE. (**M**) Elastic wave speeds in the chicken breast along the two directions, measured by UE and OCE. (**N**) Comparison between PLM-measured and known fiber orientations in a sheep tendon. Scale bars, 2 mm [(F) to (H)] and 0.5 mm [(I) to (K)]. Time intervals between two elastic wave propagation maps in (F): 1.29 ms; [(G) and (H)]: 0.43 ms; (I): 0.24 ms; and [(J) and (K)]: 0.1 ms. Panels (A) and (B) were created in BioRender. Li, R. (2023) BioRender.com.

properties in biological tissues, chicken breast was used as it is a known anisotropic material. The ultrasound array and OCT beam scanned the same chicken breast in parallel ($\theta = 0°$) and perpendicular ($\theta = 90°$) of the fiber orientation (Fig. 2B). In the anisotropic medium, chicken breast in this case, elastic waves are anticipated to propagate faster along fiber orientations (Fig. 2E). Although fiber alignment can be partially observed during ultrasound imaging, it is still necessary to quantify the biomechanical properties using elastography (fig. S9, A and B). The elastic wave propagation maps in $\theta = 0°$ direction (Fig. 2, G and J) and the maps in $\theta = 90°$ direction (Fig. 2, H and K) verified that the elastic wave was faster along with the fiber orientation. For UE measurement, the elastic wave speed in $\theta = 90°$ and $\theta = 0°$directions were 4.59 ± 0.03 and 5.72 ± 0.16 m/s, respectively (fig. S9, C and D). For OCE measurement, the elastic wave speeds were 4.2 ± 0.08 and 5.56 ± 0.03 m/s in two directions, respectively (fig. S10). The statistical data were summarized in Fig. 2M.

The PLM system was validated using a standard approach described previously (*46*). Briefly, a sheep tendon sample was imaged at multiple known orientations. The tendon had been fixed under sufficient tensile load to ensure maximum fiber alignment without inducing fiber damage (*24*). We then compared the averaged PLM-determined orientations to the actual, known orientations. Figure 2C shows PLM-colored images corresponding to four representative actual orientations. With measurements repeated in 10° increments from 0° to 180°, the accuracy of the PLM system was clearly demonstrated (Fig. 2N).

UE measurements

Elastographic measurements of the equatorial sclera were performed in four quadrants, along two orthogonal directions, and across five IOP levels using nine porcine eyes. Guided by real-time B-mode imaging, the equatorial sclera was precisely placed within the ultrasonic array's focal area. For each measurement, a specific quadrant and direction was chosen. IOP was systematically adjusted from 10 to 30 mmHg in 5-mmHg increments. After scanning one direction, the orientation was switched, and the imaging protocol was repeated for the remaining three quadrants.

From these assessments, spatial-temporal maps were generated, allowing for the computation of elastic wave speed (figs. S11 and S12). These elastic wave maps present detailed biomechanical property visualizations. To compute the wave speed, axial displacement profiles from adjacent lateral positions at the same depth were analyzed using a 1D autocorrelation algorithm to extract time delays. Given the known lateral spacing, local wave speed was calculated across the entire image. Representative fused images combining B-mode anatomy and wave speed maps are shown in Fig. 3 (A to D). To improve contrast, dual color maps were applied. Figure 3 (E to H) summarizes the measured elastic wave speeds across all IOP levels and quadrants. Anisotropy was defined as the ratio of wave speeds measured in the equatorial versus meridional directions. The corresponding anisotropy data for each quadrant at different IOP levels are presented in Fig. 3 (I to L).

OCE measurement

Similar to the UE measurements, OCE was used to assess elastic wave speeds across four quadrants of the equatorial sclera under varying directions and IOP levels, using six porcine eyes. Confocal alignment of the ultrasound excitation and OCT detection beams was achieved through real-time Doppler imaging, ensuring precise positioning of the equatorial sclera within the focal zone to optimize phase signal quality.

Elastic wave propagation maps highlighted the speed variations of wave propagation across distinct directions (fig. S13). Unlike the UE's ultrasonic array, OCE uses a noncontact approach, making 4D elastographic measurements more accessible. To achieve this, a motor controlled the azimuthal movement of the equatorial sclera. Each azimuthal position's elastic wave propagation maps were then compiled into a comprehensive 3D representation (fig. S14).

Figure 4 (A to D) displays 3D wave propagation maps acquired at 10 mmHg, highlighting directional differences in the temporal and inferior quadrants. In both regions, wave propagation was faster in the equatorial direction. Because axial displacement is related to phase shift, a stiffer medium subjected to the same acoustic force exhibits smaller phase changes. Consistent with this, we observed reduced phase shifts in the equatorial direction, corroborating the directional stiffness differences. Last, Fig. 4 (E to H) summarizes the elastic wave speeds measured across all quadrants and IOP levels, and Fig. 4 (I to L) presents the corresponding anisotropy values.

PLM, SEM, and TEM measurement

To investigate the fiber orientation of the equatorial sclera, three porcine eyes were analyzed in the PLM study. Figure 5A illustrates the definition of the equatorial and meridional directions, whereas fig. S15 shows the dissection approach: Each globe was opened into four quadrants and cut into a trapezoidal shape, with the anterior edge shorter than the posterior. This geometry preserved orientation even if surface fiducial markers were lost or became difficult to discern. Figure 5B displays a representative PLM image from the temporal quadrant. Pixel brightness indicates birefringence strength—high values reflect dense, well-aligned in-plane collagen—whereas pixel color represents local fiber orientation based on the accompanying color wheel. Although a broad distribution of fiber orientations is observed, the section shown is predominantly green, indicating a dominant meridional alignment. To assess whether depth-dependent inhomogeneities influence the observed fiber orientation patterns, we performed an in-depth analysis of PLM data by segmenting the 30-μm sections into 10 equally spaced layers from the interior to the exterior scleral surface. The orientation distributions for each depth layer were extracted and are presented in Fig. 5C. Although minor differences were observed between layers, particularly a slightly stronger anisotropy in the interior sclera, the dominant fiber orientations remained consistent throughout the depth of the tissue. This consistency suggests that the fiber alignment trends observed in our main PLM analysis are representative of the overall tissue architecture.

Orientation distributions for each quadrant are summarized in Fig. 5D. All four quadrants from one eye exhibited generally well-aligned fibers. The nasal, superior, and temporal quadrants showed a predominant meridional alignment, whereas the Inferior quadrant demonstrated a preferred orientation ~30° off the meridional axis. These plots were generated using all PLM data from each quadrant. On average, 14 sections per quadrant were analyzed (range: 8 to 19). Specifically, the number of sections used in Fig. 5D were as follows: nasal, 11; superior, 10; temporal, 9; inferior, 13. Each 30-μm-thick section yielded ~2 million measurements (orientation and birefringence energy per pixel), resulting in roughly 28 million data points per quadrant. Orientation histograms were computed with 1° resolution by weighting each orientation value by its energy and normalizing to the total number of measurements.

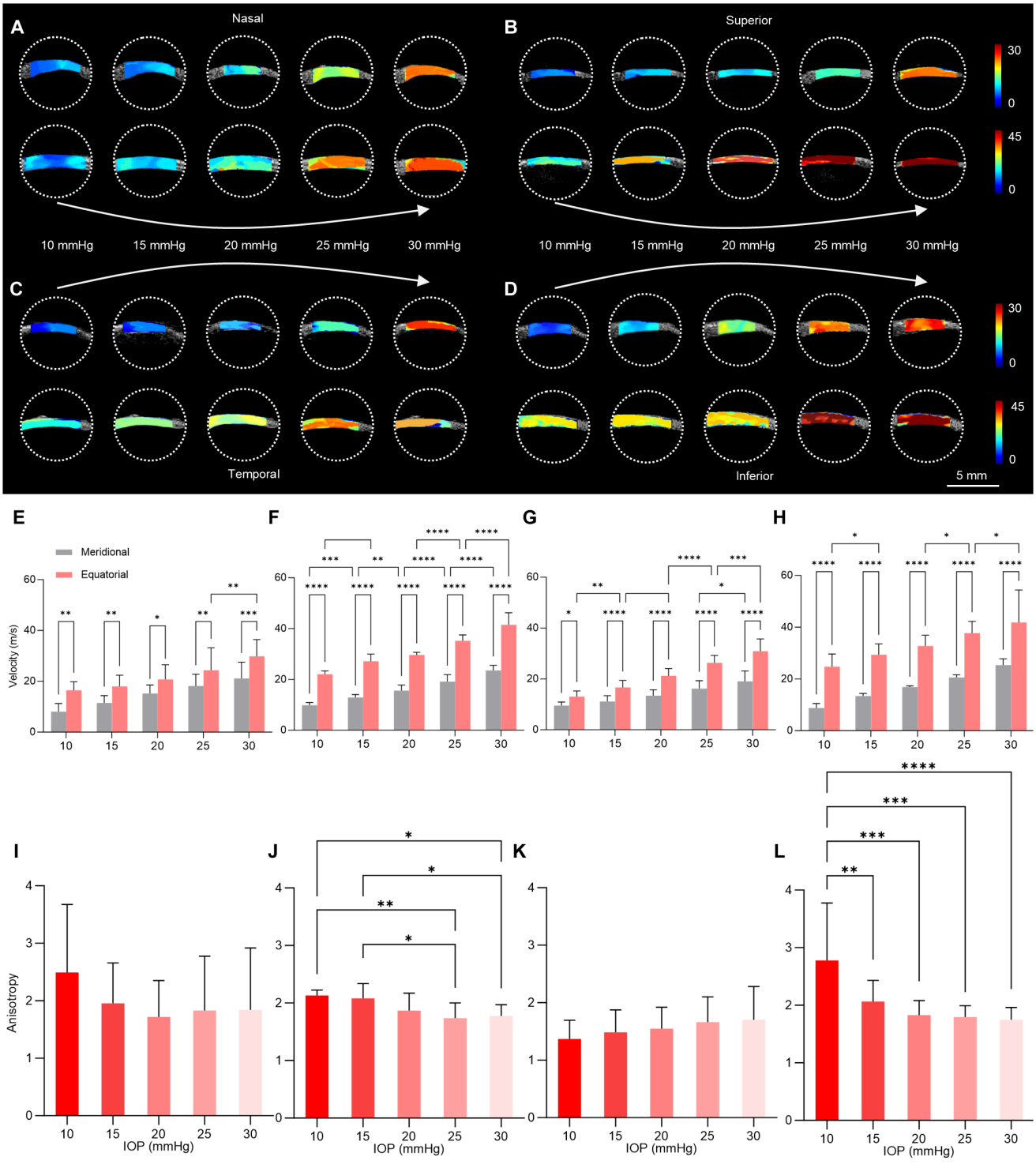

Fig. 3. Fusion images of the equatorial sclera in different quadrants, directions, and IOPs from UE measurements and statistical analysis. (**A** to **D**) Fusion images combining B-mode structural images with elastic wave speed maps in the nasal, superior, temporal, and inferior quadrants, respectively. The top and bottom rows correspond to the meridional and equatorial directions. The color map range is 0 to 30 m/s for the meridional direction and 0 to 45 m/s for the equatorial direction. Color map indicates elastic wave speed (unit: m/s). (**E** to **H**) Statistical distributions of elastic wave speeds in the meridional and equatorial directions of the equatorial sclera at varying IOP levels. (**I** to **L**) Quantitative analysis of anisotropy between the meridional and equatorial directions in the equatorial sclera at different IOPs. Quadrant mapping: [(E) and (I)] nasal; [(F) and (J)] superior; [(G) and (K)] temporal; and [(H) and (L)] inferior.

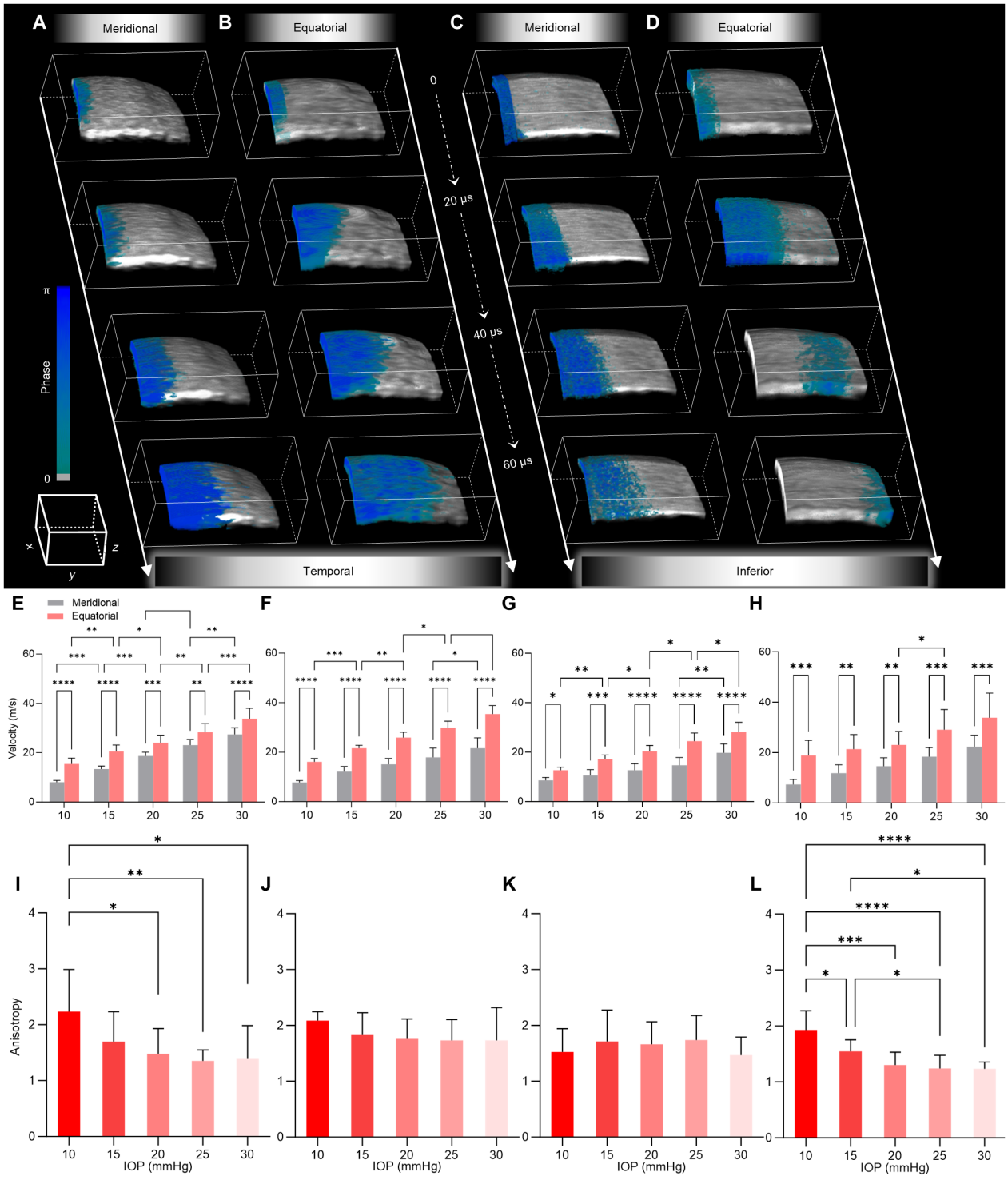

Fig. 4. 3D elastic wave propagation images of the equatorial sclera from OCE measurements and corresponding statistical analyses. 3D elastic wave propagation images of the equatorial sclera acquired using OCE at 20-μs time intervals in different quadrants and directions. (**A** and **B**) Meridional and equatorial directions in the temporal quadrant. (**C** and **D**) Meridional and equatorial directions in the inferior quadrant. (**E** to **H**) Statistical distributions of elastic wave speeds in the meridional and equatorial directions at varying IOP levels. (**I** to **L**) Quantification of anisotropy between the meridional and equatorial directions under different IOPs. [(E) and (I)] Nasal; [(F) and (J)] superior; [(G) and (K)] temporal; [(H) and (L)] inferior. Scale bar, 1 mm^3.

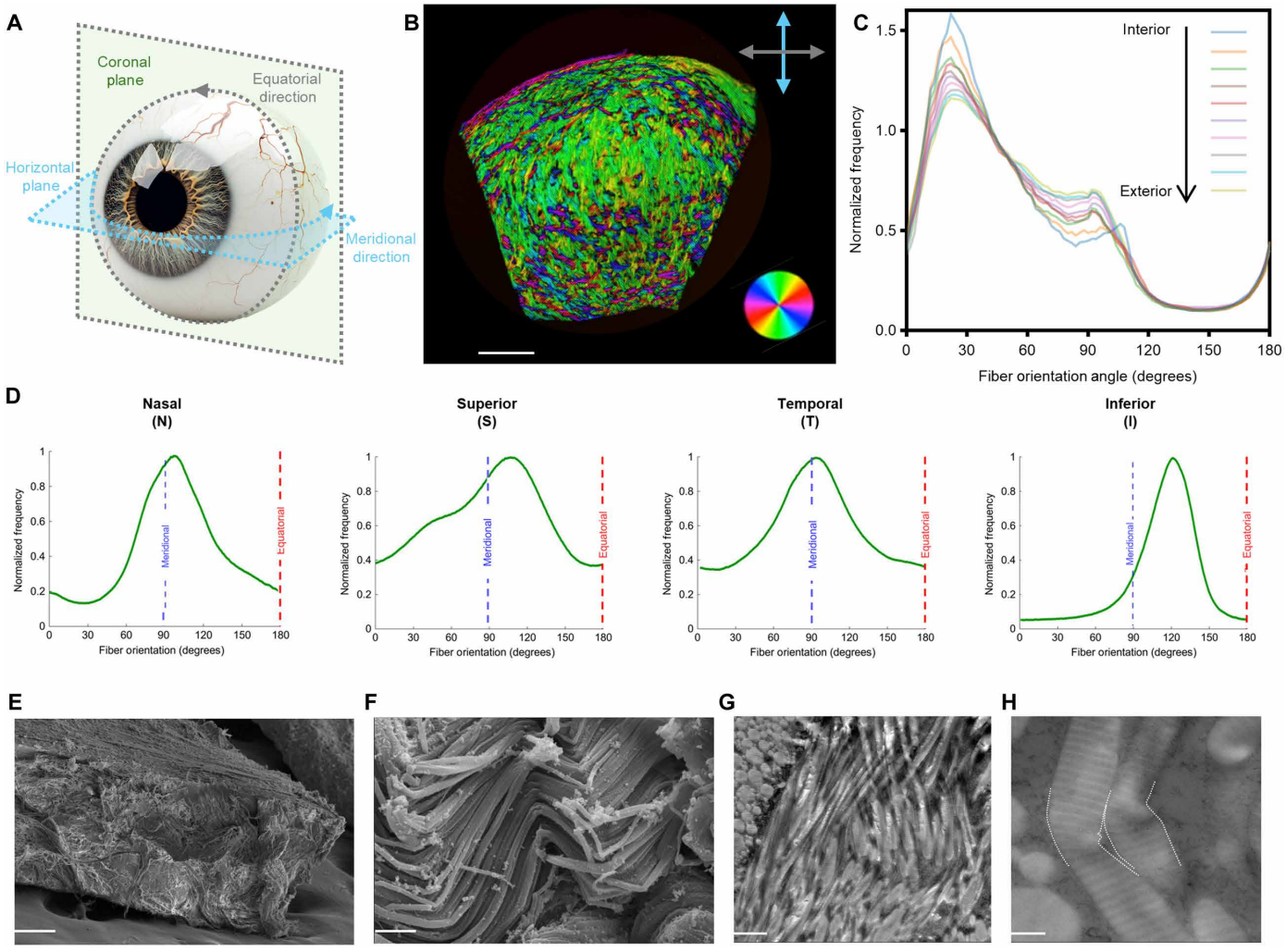

Fig. 5. Multiscale characterization of collagen architecture in the equatorial sclera. (**A**) Schematic illustrating the two principal directions in the equatorial sclera: the equatorial (circumferential) direction, corresponding to 0° and 180° (gray arrows), and the meridional (anterior-posterior) direction, corresponding to 90° (blue arrows). These orientations and color schemes are consistent across (A) to (C). (**B**) Representative PLM image of a scleral section. (**C**) Depth-resolved analysis of collagen fiber orientation in the inferior quadrant of equatorial sclera using PLM. (**D**) Orientation distributions from each of the four quadrants of a globe. Red and blue labels indicate equatorial (0° and 180°) and meridional (90°) directions, respectively. (**E** and **F**) Representative SEM images. (**G** and **H**) Representative TEM images. Scale bars, 1.5 mm (B), 0.1 mm (E), 1.5 μm (F), 1 μm (G), and 0.2 μm (H).

The SEM images in Fig. 5 (E and F) reveal that collagen fibers exhibit a woven, nonuniform alignment, suggesting complex microstructural organization. TEM images (Fig. 5, G and H) further demonstrate that collagen fibers are arranged across multiple planes, with clear evidence of twisting, interweaving, and perpendicular orientation. These features underscore the hierarchical architecture of the equatorial sclera and likely play a critical role in modulating its mechanical properties by redistributing local stress and strain.

DISCUSSION

The sclera functions as the eye's primary protective and load-bearing tissue, and its biomechanics have been investigated using a range of techniques (*51*–*54*). Given the challenges of directly measuring scleral mechanical properties in vivo, finite element modeling (FEM) is commonly used as a complementary method to simulate how the sclera responds to elevated IOP. Although FEM provides useful insights, it often relies on assumptions that may not reflect physiological conditions, such as treating surrounding scleral regions as isotropic (*55*). Uniaxial and biaxial mechanical testings have also been used to characterize the stress-strain relationship of scleral tissue (*36*). However, these methods require excising and cutting the sclera into strips, which removes physiological boundary conditions and may affect the accuracy of the measurements. Moreover, these tests do not permit manipulation of IOP during experimentation. Inflation testing enables IOP modulation, but it only provides relative strain changes and does not offer direct measurement of stiffness (*56*).

Elastography was extensively used in this study to investigate the mechanical properties of the equatorial sclera under different quadrants and conditions. In this study, we did not convert wave speed to Young's modulus due to limitations posed by physical conditions such as unrealistic assumptions of the biological tissues (*57*). This

topic is challenging and beyond the scope of this study. Nevertheless, it is clear that the elastic wave speed is positively correlated with the mechanical properties.

For UE and OCE measurements, inherent variability among the samples must be considered. Factors such as age influence the mechanical properties of the sclera, introducing variability in measurements. In addition, within the equatorial sclera, nonhomogeneity and variations in properties like thickness and curvature also affect the elastic wave speed. Given these complexities, the data on elastic wave speed and anisotropy may not show statistical significance, and a definitive linear regression model was not asserted on the relationship between elastic wave speed and IOP levels. Moreover, quadrant-to-quadrant comparisons of anisotropy were not performed as such analyses would require detailed anatomical control and fall beyond the scope of the present study. For instance, UE measurements in this study involved scanning only a single azimuthal position per quadrant due to hardware limitations. Because scleral thickness and curvature vary along the azimuthal axis, measurements from one location cannot be assumed to represent the mechanical behavior of the entire quadrant, making intraquadrant comparisons unreliable. Instead, our experimental design focused on comparing elastic wave propagation along orthogonal directions (meridional versus equatorial) within the same quadrant. This approach minimizes the influence of local geometric variability and allows directional differences in wave speed to be primarily attributed to differences in mechanical properties, such as collagen fiber orientation. Therefore, we believe that the observed directional differences in wave speed primarily reflect differences in mechanical properties, such as collagen fiber orientation, rather than geometric effects. Future work using larger sample sizes, controlled anatomical stratification, and multidirectional elastographic scanning with coregistered thickness and curvature mapping will be essential to better understand how elastic wave speed relates to geometry, quadrant, and IOP.

A sclera that is mechanically softer in the meridional direction may predispose the eye to elongate along the anterior-posterior axis in response to elevated IOP, without a corresponding increase in equatorial diameter. This hypothesis aligns with prior MRI findings showing that the equatorial diameter of sheep eyes remained unchanged as IOP increased from 0 to 40 mmHg (*12*). Such a behavior may be relevant to the pathophysiology of myopia, where the sclera undergoes substantial, often irreversible, axial elongation (*14*). As IOP increases, the anisotropy of the equatorial sclera may also change, suggesting an adaptive mechanism by which the tissue redistributes mechanical stress. These findings highlight the potential role of the equatorial sclera in protecting the globe under load and its contribution to ocular structural integrity in the context of glaucoma progression.

It was unexpected to find that the equatorial sclera mechanical anisotropy did not concur with the primary collagen fiber orientations observed with PLM. This mismatch was particularly pronounced in the superior and inferior quadrants, although some level of discrepancy was evident in all quadrants. The origin of this divergence remains uncertain. One possibility is that not all collagen fibers contribute equally to mechanical stiffness. For example, meridional fibers may be more compliant than circumferential fibers, potentially due to greater crimp, which delays their recruitment under stretch. Alternatively, meridional fibers might be thinner or less densely packed but still exhibit similar birefringence, thereby masking structural differences in PLM. Despite differing in excitation mechanisms, spatial resolution, and coupling conditions, both UE and OCE yielded consistent anisotropy patterns across independent samples. This cross-modal agreement supports the conclusion that the observed mechanical anisotropy is not a methodological artifact but rather an intrinsic property of the equatorial sclera.

In this study, we used 30-μm-thick cryosections for PLM imaging. This thickness was chosen to balance two important factors: maintaining sufficient signal strength for accurate birefringence detection and minimizing artifacts caused by mechanical distortion during sectioning. Because PLM is based on transmitted light, each pixel's orientation measurement reflects the cumulative optical properties along the full depth of the section (*46*, *47*). Although our previous study has demonstrated that orientation measurements from 30-μm-thick sections are accurate to within a few degrees, we acknowledge that local inhomogeneities in scleral composition and lamellar organization may still introduce small deviations (*33*). As a result, the orientation distributions reported here should be interpreted as approximations, accurate to within a few degrees of the true in-plane fiber architecture. To further assess whether depth-dependent variation might influence our findings, we performed a depth-resolved analysis by dividing each 30-μm section into 10 equally spaced layers (Fig. 5C). Although slight variations in anisotropy were observed—particularly a trend toward stronger alignment in the interior layers—the dominant fiber orientation remained consistent across the full depth of the tissue. This result supports the interpretation that our measurements reliably capture the principal orientation trends and are not significantly biased by through-thickness variation. Together, these analyses validate the use of 30-μm sections for characterizing fiber orientation in equatorial sclera. Nonetheless, future studies may benefit from either thinner sections or advanced volumetric imaging and computational approaches that can better account for tissue heterogeneity and 3D architecture (*58*, *59*).

A comprehensive set of approaches was used to characterize the equatorial sclera, spanning mechanical response and collagen fiber orientation. The equatorial sclera was evaluated across four quadrants, two directions, and five different IOP levels. Four key findings emerged from this study: First, the equatorial sclera was consistently stiffer in the equatorial direction, confirming mechanical anisotropy. Second, this mechanical anisotropy did not align with the dominant collagen fiber orientations identified by PLM. Third, the degree of anisotropy varied across quadrants and with changing IOP. Fourth, the elastic wave speed increased linearly with IOP in both directions, suggesting that the equatorial sclera exhibits a pressure-dependent biomechanical response similar to that of the posterior sclera. Together, these findings help explain how the equatorial sclera accommodates elevated IOP without large equatorial expansion, why axial elongation dominates in myopia, and what mechanical benchmarks should guide the design of rapid ocular sealants.

There are several limitations to this study. First, all measurements were performed on ex vivo porcine eyes, and in vivo validation remains lacking. This limitation is primarily due to the size and mounting constraints of the ultrasonic array, which currently makes perpendicular placement at specific eye locations challenging. OCE, with its noncontact nature and smaller footprint, has greater potential for in vivo application and will be explored in future studies. Second, measurements were limited to two orthogonal directions per quadrant rather than a full range of angles. This constraint stems from the use of a linear array transducer, which does not easily permit angular manipulation. A 2D matrix array could overcome this limitation by enabling targeted imaging across multiple planes and directions. Third,

although the OCE system enabled the acquisition of volumetric (4D) data, the high data volume posed a bottleneck for full-scale processing. For each quadrant, IOP level, and propagation direction, 300 azimuthal positions were scanned with a 10-μm step size. Although we did not analyze the entire dataset, the reconstructed 3D elastic wave propagation images (e.g., Fig. 4, A and B) already reveal azimuthal variations in wave speed that may correlate with local fiber alignment and structural anisotropy. To facilitate comprehensive data utilization in future studies, we plan to implement autonomous, high-throughput processing algorithms. Last, the mechanical anisotropy and structural anisotropy were measured in different sets of eyes. Because both procedures obtained fairly consistent measurements across globes, it seems unlikely that the discrepancies are because of interglobe variability. Nevertheless, the possibility remains, and future studies should be done on the same globe. We posit that a discrepancy between mechanical and microstructural anisotropy is potentially crucial to understanding the eye and the effectiveness of UE and OCE techniques, even if it only occurs sporadically. Despite these limitations, our results consistently demonstrate that the anisotropy of the equatorial sclera is not an artifact of imaging modality, geometry, or specimen variability. Instead, it appears to be an intrinsic property governed by collagen fiber architecture and local microstructure.

MATERIALS AND METHODS

Imaging phantom, chicken breast, and sheep tendon preparation for validation

The imaging phantom was fabricated to validate the accuracy of the UE and OCE systems. Gelatin (Gelatin G8-500, Fisher Scientific, USA) was used to control stiffness, and silicon carbide powder (S5631, Sigma-Aldrich, St. Louis, MO, USA) was added for acoustic scattering, Intralipid was included for optical scattering, and 1-propanol (9086-01, J.T. Baker, Center Valley, PA, USA) was incorporated to adjust sound speed.

Chicken breast tissue was obtained from a local vendor. The dominant fiber orientation was visually identified on the tissue surface, and fiducial markers were placed in two orthogonal directions to ensure consistent alignment during UE and OCE measurements.

Sheep Achilles tendons were acquired from a local abattoir, rinsed in phosphate-buffered saline (PBS), and dissected into thin strips for analysis (*24*). The strips were mounted in a custom uniaxial loading device and stretched until all visible collagen crimp patterns disappeared while avoiding fiber failure. While under tension, the tissues were immersion fixed in 10% formalin for 1 hour. Following fixation, formalin was replaced with PBS and the load was released. Samples were cryoprotected in 30% sucrose, sectioned into 30-μm slices, washed in PBS, and mounted onto glass slides for imaging.

Porcine eye preparation for the measurements

All experiments were conducted on the same day upon receiving of the porcine eyes. Unscalded porcine eyes used for UE and OCE measurements were obtained from a research-grade vendor (Sierra for Medical Science, Whittier, CA, USA). A total of nine eyes were used for UE and six eyes for OCE. The specimen preparation procedures were identical for both elastography methods. The conjunctiva and surrounding tissues, including the muscle, were removed using a blade, whereas the globe remained intact. Eyes were then secured in a custom-designed holder for imaging. To control and monitor the IOP, two 23-gauge trocars (Bausch & Lomb, Bridgewater, NJ, USA) were inserted into the posterior sclera ~1.5 mm adjacent to the ONH to establish ports. An infusion line that contained balanced salt solution (BSS) was inserted into one port, and IOP can be controlled by changing the height of the infusion line. A pressure sensor (model SPR-524, Millar Inc., Pearland, TX, USA) was inserted to the other port to monitor the IOP level in real time. Air bubbles occasionally entered the globe during IOP manipulation—either through the infusion line or access ports in the equatorial sclera—and interfered with wave propagation. If present, these bubbles tended to float toward and adhere to the scleral surface, leading to disruption of elastic wave transmission. Spatial-temporal maps exhibiting reversed wavefront directions, inconsistent propagation, or other anomalies were deemed artifactual and excluded from analysis. For each IOP level, direction, and quadrant, three measurements were performed. To ensure consistency between UE and OCE results, only one verified, artifact-free dataset was retained for analysis per condition. In UE measurements, the mechanical shaker was placed perpendicular to the scleral surface and aligned with the imaging array within the same plane. For PLM measurements, three unscalded porcine eyes from three animals were obtained from a local slaughterhouse in Pittsburgh. The globes were cleaned of external tissues, and square samples (~11 mm by 11 mm) of equatorial sclera were dissected from the superior, inferior, nasal, and temporal quadrants. Samples were trimmed into trapezoidal shapes with the anterior side shorter than the posterior to preserve orientation during processing. Tissues were fixed in 10% formalin for 2 hours and cryosectioned into 30-μm-thick sections.

UE data collection and processing

The Vantage 256 system was used to control the linear array transducer and synchronize the elastography system. The platform generated a trigger signal sent to a function generator (AFG 3252C, Tektronix, Beaverton, OR, USA), which was connected to a power amplifier (type 2718, Brüel & Kjær, Duluth, GA, USA). The amplifier drove a mechanical shaker (type 4810, Brüel & Kjær) that delivered a single-cycle pulse at 1 kHz (1-ms duration) to initiate elastic wave propagation.

A rigid rod with a diameter of 0.3 mm was affixed to the shaker and aligned within the imaging plane of the array. It was positioned perpendicular to the tissue surface to apply localized indentation and generate elastic wave propagation. Because of the simultaneous A-line acquisition capability of the 128-element linear array, only a single vibration was required to capture the full wave propagation across the FOV.

Both B-mode imaging and ultrafast elastography were performed using an 18-MHz linear array transducer (L22-14v, Verasonics, Kirkland, WA, USA) with a −6-dB bandwidth of 67%, as specified by the manufacturer. The pulse repetition frequency (PRF) was set to 7 kHz to enable high–temporal resolution tracking of the elastic wave. Three-angle plane wave compounding was used to enhance image quality and displacement sensitivity.

After each scan, the IQ data were saved for offline processing. Axial displacement Δd was estimated using the 1D autocorrelation method, based on the phase shift $\Delta\varphi$ between two consecutive A-lines

$$\Delta d = \frac{\Delta\varphi}{2\pi} \cdot \lambda \quad (1)$$

where $\lambda = c/f$ is the axial wavelength, f is the center frequency of the ultrasound transducer, and c is the longitudinal wave speed and is typically 1540 m/s in soft tissue.

A 3D data matrix was reconstructed, containing the lateral position, depth position, and time, with axial displacement as the value at each voxel. To calculate the elastic wave speed, spatial-temporal maps (axial displacement versus lateral position and time) were generated at each depth. These maps were averaged along the depth direction of the equatorial sclera to improve signal-to-noise ratio (SNR) and measurement accuracy.

Elastic wave speed was estimated by calculating the slope of the wavefront in the averaged spatial-temporal maps. Linear regression was applied to the peak axial displacements across lateral positions to determine propagation time delays. Known propagation distances and calculated time delays were used to compute the elastic wave speed.

For localized elastic wave speed mapping across four quadrants, two imaging directions, and five IOP levels, additional steps were performed. The 3D data matrix was first interpolated in the time domain to refine temporal resolution. Then, axial displacement time series between adjacent lateral positions was autocorrelated to calculate local time shifts, enabling point-by-point reconstruction of localized elastic wave speeds at each depth. Gaussian and median filters were applied to the resulting localized maps to further enhance signal quality.

OCE data collection and processing

A custom phase-resolved spectral-domain OCT (SD-OCT) system integrated with a 6.8-MHz ring transducer was used for elastic wave detection and excitation, respectively. The OCT beam had a center wavelength of 890 nm, a bandwidth of 144 nm, and an output power of 9 mW. A superluminescent diode (Superlum Diodes Ltd., Carrigtwohill, Co. Cork, Ireland) provided the light source, with a 20/80 optical coupler splitting the beam into sample and reference arms. Lateral scanning for OCE was performed using a dual-axis galvanometer with a 3-μm step size across 1000 lateral positions. At each position, a 2-ms acoustic radiation force (ARF) burst was applied using a ring transducer to induce elastic wave propagation. The transducer was driven by a function generator and a power amplifier (100A250A, AR RF/Microwave Instrumentation, Souderton, PA, USA). Because OCT acquisition is point-by-point, a separate ARF excitation was required at each lateral location. The resulting wave propagation was tracked by OCT through 400 A-lines per position, forming M-B mode data used to reconstruct spatial-temporal displacement maps. The A-line acquisition rate was 50 kHz, and the entire OCE system was synchronized by a global clock to ensure temporal consistency across measurements.

The ring transducer used for ARF generation was custom fabricated, with its piezoelectric material composed of modified PZT-4 ceramic. It had an aperture of 23 mm and a central hole diameter of 10 mm (fig. S16). A two-way pulse-echo test was performed to characterize its acoustic properties. The transducer was immersed in deionized, degassed water and mounted on customized translation stages with five degrees of freedom. A quartz plate placed beneath the transducer served as the acoustic reflector. The transducer was driven by a pulser receiver (JSR500, Ultrasonics, Pittsford, NY, USA) at a PRF of 20 kHz. rf signals were captured using a 12-bit digitizer (ATS9360, Alazartech, Montreal, QC, Canada) at a sampling rate of 1.8 GHz for offline analysis. The focal distance was determined to be 23.17 mm based on the time-of-flight corresponding to the maximum echo signal. The −6-dB bandwidth, obtained from the Fourier transform of the echo waveform, was 12.07%.

Acoustic field measurements were carried out using a hydrophone (HGL-0085, ONDA Corporation, Sunnyvale, CA, USA), with data recorded by the same digitizer. The measured −3-dB lateral and axial beam widths were 0.22 and 1.97 mm, respectively. After calibrating the acoustic output with a hydrophone, the derated mechanical index was determined to be 1.48 during OCE measurements.

Axial displacements were extracted by calculating the phase shift $\Delta\varphi$ between consecutive A-lines

$$\Delta\varphi = arg\left(I_m \times I_{m+1}^{*}\right) \tag{2}$$

where I_m and I_{m+1} represents the complex signal at the same depth of two consecutive A-lines, and I_{m+1}^{*} represents the complex conjugate. The axial displacement Δd resulting from the elastic wave was calculated by

$$\Delta d = \frac{\lambda \Delta\varphi}{4\pi n} \tag{3}$$

where λ is the center wavelength of the OCT system, and n is the refractive index of the tissue. Spatial-temporal displacement profiles were visualized in M-B mode to capture elastic wave propagation.

PLM data collection and processing

In PLM, linear polarizer filters are placed before and after samples. In this case, the samples were histological cryosections of pig equatorial sclera. Images at multiple filter orientations 45° apart were acquired using a dissecting upright microscope (MVX10 MacroView Zoom Microscope, Olympus Corporation, Tokyo, Japan) with a Hamamatsu Flash 4.0 LT and a 1x objective numerical aperture of 0.25, at an effective magnification of 0.8x for a resolution of 4.02 μm per pixel. Four filter orientations were used for each section to quantify collagen crimp orientation at each pixel.

For analysis, orientation distributions were first computed for each section and then integrated over the volume. A masking technique was used to focus the quantitative analysis on collagenous tissues that were primarily aligned in the plane of the sclera (*46*). This was done by computing an energy parameter. The energy signal was small where there is no collagen, such as outside of the sample, or if fibers have a large inclination relative to the local plane. In the equatorial sclera, most of the fibers are well aligned with the scleral shell plane (*60*). The energy parameter was particularly helpful for the visualization by making tissue regions easily distinguishable from the background.

Multiple sections were obtained from each eye, with the number of sections varying depending on local tissue thickness and curvature. On average, each sample yielded 14 sections (range: 8 to 19). All sections obtained from each sample were included in the analysis. To obtain a representative orientation distribution for a given sample, orientation data from all sections were combined.

Statistical analysis

The UE data were processed by MATLAB 2021a (MathWorks, Natick, MA, USA); OCE data were processed by MATLAB 2021a, ImageJ (National Institutes of Health, Bethesda, MD, USA); and PLM images were processed using custom code in Fiji (*61*). Error bar denotes means ± SD. The statistical analysis was conducted by ordinary one-way analysis of variance (ANOVA), and linear regression was performed in

the corresponding sections. Significance values were labeled with no significance (n.s.), $*P < 0.05$, $**P < 0.01$, $***P < 0.001$, and $****P < 0.0001$.

Supplementary Materials

This PDF file includes:

Supplementary Notes 1 to 3
Figs. S1 to S16
References

REFERENCES AND NOTES

1. T. M. Nguyen, J. F. Aubry, M. Fink, J. Bercoff, M. Tanter, In vivo evidence of porcine cornea anisotropy using supersonic shear wave imaging. *Invest. Ophthalmol. Vis. Sci.* **55**, 7545–7552 (2014).
2. J. Heys, V. H. Barocas, Mechanical characterization of the bovine iris. *J. Biomech.* **32**, 999–1003 (1999).
3. J. Zhang, J. Murgoitio-Esandi, X. Qian, R. Li, C. Gong, A. Nankali, L. Hao, B. Y. Xu, K. Kirk Shung, A. Oberai, Q. Zhou, High-frequency ultrasound elastography to assess the nonlinear elastic properties of the cornea and ciliary body. *IEEE Trans. Ultrason. Ferroelectr. Freq. Control* **69**, 2621–2629 (2022).
4. J. F. Koretz, G. H. Handelman, A model for accommodation in the young human eye: The effects of lens elastic anisotropy on the mechanism. *Vision Res.* **23**, 1679–1686 (1983).
5. K. Chen, J. D. Weiland, Anisotropic and inhomogeneous mechanical characteristics of the retina. *J. Biomech.* **43**, 1417–1421 (2010).
6. R. Grytz, M. A. Fazio, M. J. Girard, V. Libertiaux, L. Bruno, S. Gardiner, C. A. Girkin, J. C. Downs, Material properties of the posterior human sclera. *J. Mech. Behav. Biomed. Mater.* **29**, 602–617 (2014).
7. A. Elsheikh, B. Geraghty, D. Alhasso, J. Knappett, M. Campanelli, P. Rama, Regional variation in the biomechanical properties of the human sclera. *Exp. Eye Res.* **90**, 624–633 (2010).
8. I. A. Sigal, J. G. Flanagan, C. R. Ethier, Factors influencing optic nerve head biomechanics. *Invest. Ophthalmol. Vis. Sci.* **46**, 4189–4199 (2005).
9. I. A. Sigal, J. G. Flanagan, I. Tertinegg, C. R. Ethier, Finite element modeling of optic nerve head biomechanics. *Invest. Ophthalmol. Vis. Sci.* **45**, 4378–4387 (2004).
10. B. Coudrillier, C. Boote, H. A. Quigley, T. D. Nguyen, Scleral anisotropy and its effects on the mechanical response of the optic nerve head. *Biomech. Model. Mechanobiol.* **12**, 941–963 (2013).
11. B. Coudrillier, J. Tian, S. Alexander, K. M. Myers, H. A. Quigley, T. D. Nguyen, Biomechanics of the human posterior sclera: Age- and glaucoma-related changes measured using inflation testing. *Invest. Ophthalmol. Vis. Sci.* **53**, 1714–1728 (2012).
12. A. P. Voorhees, L. C. Ho, N. J. Jan, H. Tran, Y. van der Merwe, K. Chan, I. A. Sigal, Whole-globe biomechanics using high-field MRI. *Exp. Eye Res.* **160**, 85–95 (2017).
13. N. A. McBrien, A. Gentle, Role of the sclera in the development and pathological complications of myopia. *Prog. Retin. Eye Res.* **22**, 307–338 (2003).
14. R. Grytz, H. Yang, Y. Hua, B. C. Samuels, I. A. Sigal, Connective tissue remodeling in myopia and its potential role in increasing risk of glaucoma. *Curr. Opin. Biomed. Eng.* **15**, 40–50 (2020).
15. I. G. Morgan, K. Ohno-Matsui, S.-M. Saw, Myopia. *Lancet* **379**, 1739–1748 (2012).
16. J. A. S. Rada, S. Shelton, T. T. Norton, The sclera and myopia. *Exp. Eye Res.* **82**, 185–200 (2006).
17. N. A. McBrien, A. I. Jobling, A. Gentle, Biomechanics of the sclera in myopia: Extracellular and cellular factors. *Optom. Vis. Sci.* **86**, E23–E30 (2009).
18. J. M. Dunkin, A. V. Crum, R. S. Swanger, S. A. J. Bokhari, Globe trauma. *Semin. Ultrasound CT MR* **32**, 51–56 (2011).
19. D. L. Cruvinel Isaac, V. C. Ghanem, M. A. Nascimento, M. Torigoe, N. Kara-José, Prognostic factors in open globe injuries. *Ophthalmologica* **217**, 431–435 (2003).
20. N. Bayat, Y. Zhang, P. Falabella, R. Menefee, J. J. Whalen III, M. S. Humayun, M. E. Thompson, A reversible thermoresponsive sealant for temporary closure of ocular trauma. *Sci. Transl. Med.* **9**, eaan3879 (2017).
21. P. M. Pinsky, D. van der Heide, D. Chernyak, Computational modeling of mechanical anisotropy in the cornea and sclera. *J. Cataract Refract. Surg.* **31**, 136–145 (2005).
22. S. L.-Y. Woo, A. S. Kobayashi, W. A. Schlegel, C. Lawrence, Nonlinear material properties of intact cornea and sclera. *Exp. Eye Res.* **14**, 29–39 (1972).
23. C. Braunsmann, C. M. Hammer, J. Rheinlaender, F. E. Kruse, T. E. Schaffer, U. Schlötzer-Schrehardt, Evaluation of lamina cribrosa and peripapillary sclera stiffness in pseudoexfoliation and normal eyes by atomic force microscopy. *Invest. Ophthalmol. Vis. Sci.* **53**, 2960–2967 (2012).
24. L. C. Ho, I. A. Sigal, N. J. Jan, A. Squires, Z. Tse, E. X. Wu, S. G. Kim, J. S. Schuman, K. C. Chan, Magic angle-enhanced MRI of fibrous microstructures in sclera and cornea with and without intraocular pressure loading. *Invest. Ophthalmol. Vis. Sci.* **55**, 5662–5672 (2014).
25. X. Qian, R. Li, G. Lu, L. Jiang, H. Kang, K. K. Shung, M. S. Humayun, Q. Zhou, Ultrasonic elastography to assess biomechanical properties of the optic nerve head and peripapillary sclera of the eye. *Ultrasonics* **110**, 106263 (2021).
26. M. M. Doyley, K. J. Parker, Elastography: General principles and clincial applications. *Ultrasound Clin.* **9**, 1–11 (2014).
27. R. Li, X. Qian, C. Gong, J. Zhang, Y. Liu, B. Xu, M. S. Humayun, Q. Zhou, Simultaneous assessment of the whole eye biomechanics using ultrasonic elastography. *IEEE Trans. Biomed. Eng.* **70**, 1310–1317 (2023).
28. F. Zvietcovich, P. Pongchalee, P. Meemon, J. P. Rolland, K. J. Parker, Reverberant 3D optical coherence elastography maps the elasticity of individual corneal layers. *Nat. Commun.* **10**, 4895 (2019).
29. R. Z. Li, Z. Du, X. Qian, Y. Li, J.-C. Martinez-Camarillo, L. Jiang, M. S. Humayun, Z. Chen, Q. Zhou, High resolution optical coherence elastography of retina under prosthetic electrode. *Quant. Imag. Med. Surg.* **11**, 918–927 (2021).
30. X. Qian, R. Li, Y. Li, G. Lu, Y. He, M. S. Humayun, Z. Chen, Q. Zhou, *In vivo* evaluation of posterior eye elasticity using shaker-based optical coherence elastography. *Exp. Biol. Med.* **245**, 282–288 (2020).
31. G. Lu, R. Li, X. Qian, R. Chen, L. Jiang, Z. Chen, K. K. Shung, M. S. Humayun, Q. F. Zhou, Layer-specific ultrasound elastography using a multi-layered shear wave dispersion model for assessing the viscoelastic properties. *Phys. Med. Biol.* **66**, 035003 (2021).
32. F. Zhang, R. Li, Y. Li, Z. Zhu, Q. Zhou, Z. Chen, Quantitative optical coherence elastography of the optic nerve head in vivo. *IEEE Trans. Biomed. Eng.* **71**, 732–737 (2024).
33. C. Boote, I. A. Sigal, R. Grytz, Y. Hua, T. D. Nguyen, M. J. A. Girard, Scleral structure and biomechanics. *Prog. Retin. Eye Res.* **74**, 100773 (2020).
34. B. Yang, N. J. Jan, B. Brazile, A. Voorhees, K. L. Lathrop, I. A. Sigal, Polarized light microscopy for 3-dimensional mapping of collagen fiber architecture in ocular tissues. *J. Biophotonics* **11**, e201700356 (2018).
35. B. Yang, P. Y. Lee, Y. Hua, B. Brazile, S. Waxman, F. Ji, Z. Zhu, I. A. Sigal, Instant polarized light microscopy for imaging collagen microarchitecture and dynamics. *J. Biophotonics* **14**, e202000326 (2021).
36. A. Eilaghi, J. G. Flanagan, I. Tertinegg, C. A. Simmons, G. W. Brodland, C. R. Ethier, Biaxial mechanical testing of human sclera. *J. Biomech.* **43**, 1696–1701 (2010).
37. R. Li, X. Qian, G. Lu, M. S. Humayun, I. A. Sigal, Q. Zhou, Research the anisotropy property in equator sclera using high frequency ultrasonic elastography. *Invest. Ophthalmol. Vis. Sci.* **62**, 2313–2313 (2021).
38. R. Li, S. Waxman, Y. Hua, F. F. Zhang, Y. Li, Y. Zhu, X. Qian, Z. Chen, Q. Zhou, I. Sigal, "Equatorial sclera anisotropy measured using ultrasound elastography," in *SPIE BiOS* (SPIE, 2021), vol. 11645.
39. F. Zhang, Y. Li, Y. Zhu, R. Li, S. Waxman, Q. Zhou, I. Sinal, Z. Chen, "Measurement of equatorial sclera mechanical anisotropy of using acoustic radiation force optical coherence elastography," in *SPIE BiOS* (SPIE, 2021), vol. 11655.
40. L. Villegas, F. Zvietcovich, S. Marcos, J. S. Birkenfeld, Revealing regional variations in scleral shear modulus in a rabbit eye model using multi-directional ultrasound optical coherence elastography. *Sci Rep.* **14**, 21010 (2024).
41. Y. Hua, M. Quinn, F. Ji, S. Salinas, R. Amini, I. A. Sigal, Mechanical anisotropy of the equatorial sclera does not concur with its preferred fiber orientation. *Invest. Ophthalmol. Vis. Sci.* **63**, 2731-A0095 (2022).
42. M. J. A. Girard, A. Dahlmann-Noor, S. Rayapureddi, J. A. Bechara, B. M. E. Bertin, H. Jones, J. Albon, P. T. Khaw, C. R. Ethier, Quantitative mapping of scleral fiber orientation in normal rat eyes. *Invest. Ophthalmol. Vis. Sci.* **52**, 9684–9693 (2011).
43. Y. Li, J. Zhu, J. J. Chen, J. X. Yu, Z. Jin, Y. S. Miao, A. W. Browne, Q. F. Zhou, Z. P. Chen, Simultaneously imaging and quantifying in vivo mechanical properties of crystalline lens and cornea using optical coherence elastography with acoustic radiation force excitation. *APL Photonics* **4**, 106104 (2019).
44. Z. Du, R. Li, X. Qian, G. Lu, Y. Li, Y. He, Y. Qu, L. Jiang, Z. Chen, M. S. Humayun, Z. Chen, Q. Zhou, Quantitative confocal optical coherence elastography for evaluating biomechanics of optic nerve head using Lamb wave model. *Neurophotonics* **6**, 041112 (2019).
45. X. J. Qian, T. Ma, C. C. Shih, M. Heur, J. Zhang, K. K. Shung, R. Varma, M. S. Humayun, Q. F. Zhou, Ultrasonic microelastography to assess biomechanical properties of the cornea. *IEEE Trans. Biomed. Eng.* **66**, 647–655 (2019).
46. N. J. Jan, J. L. Grimm, H. Tran, K. L. Lathrop, G. Wollstein, R. A. Bilonick, H. Ishikawa, L. Kagemann, J. S. Schuman, I. A. Sigal, Polarization microscopy for characterizing fiber orientation of ocular tissues. *Biomed. Opt. Express* **6**, 4705–4718 (2015).
47. N. J. Jan, K. Lathrop, I. A. Sigal, Collagen architecture of the posterior pole: High-resolution wide field of view visualization and analysis using polarized light microscopy. *Invest. Ophthalmol. Vis. Sci.* **58**, 735–744 (2017).
48. H. Tran, N. J. Jan, D. Hu, A. Voorhees, J. S. Schuman, M. A. Smith, G. Wollstein, I. A. Sigal, Formalin fixation and cryosectioning cause only minimal changes in shape or size of ocular tissues. *Sci. Rep.* **7**, 12065 (2017).
49. A. Gogola, N. J. Jan, B. Brazile, P. Lam, K. L. Lathrop, K. C. Chan, I. A. Sigal, Spatial patterns and age-related changes of the collagen crimp in the human cornea and sclera. *Invest. Ophthalmol. Vis. Sci.* **59**, 2987–2998 (2018).

50. A. Gogola, N. J. Jan, K. L. Lathrop, I. A. Sigal, Radial and circumferential collagen fibers are a feature of the peripapillary sclera of human, monkey, pig, cow, goat, and sheep. *Invest. Ophthalmol. Vis. Sci.* **59**, 4763–4774 (2018).
51. M. E. Hamdaoui, A. M. Levy, A. B. Stuber, C. A. Girkin, T. W. Kraft, B. C. Samuels, R. Grytz, Scleral crosslinking using genipin can compromise retinal structure and function in tree shrews. *Exp. Eye Res.* **219**, 109039 (2022).
52. L. Zhang, J. Albon, H. Jones, C. L. Gouget, C. R. Ethier, J. C. Goh, M. J. Girard, Collagen microstructural factors influencing optic nerve head biomechanics. *Invest. Ophthalmol. Vis. Sci.* **56**, 2031–2042 (2015).
53. A. P. Voorhees, N. J. Jan, Y. Hua, B. Yang, I. A. Sigal, Peripapillary sclera architecture revisited: A tangential fiber model and its biomechanical implications. *Acta Biomater.* **79**, 113–122 (2018).
54. Y. Hua, A. P. Voorhees, N. J. Jan, B. Wang, S. Waxman, J. S. Schuman, I. A. Sigal, Role of radially aligned scleral collagen fibers in optic nerve head biomechanics. *Exp. Eye Res.* **199**, 108188 (2020).
55. R. E. Norman, J. G. Flanagan, I. A. Sigal, S. M. K. Rausch, I. Tertinegg, C. R. Ethier, Finite element modeling of the human sclera: Influence on optic nerve head biomechanics and connections with glaucoma. *Exp. Eye Res.* **93**, 4–12 (2011).
56. K. M. Myers, B. Coudrillier, B. L. Boyce, T. D. Nguyen, The inflation response of the posterior bovine sclera. *Acta Biomater.* **6**, 4327–4335 (2010).
57. A. Baghani, S. Salcudean, R. Rohling, Theoretical limitations of the elastic wave equation inversion for tissue elastography. *J. Acoust. Soc. Am.* **126**, 1541–1551 (2009).
58. X. Liu, L. Jiang, M. Ke, I. A. Sigal, J. Chua, Q. V. Hoang, A. W. Chia, R. P. Najjar, B. Tan, J. Cheong, V. Bellemo, R. S. Chong, M. J. A. Girard, M. Ang, M. Liu, G. Garhofer, V. A. Barathi, S.-M. Saw, M. Villiger, L. Schmetterer, Posterior scleral birefringence measured by triple-input polarization-sensitive imaging as a biomarker of myopia progression. *Nat. Biomed. Eng.* **7**, 986–1000 (2023).
59. B. Yang, B. Brazile, N. J. Jan, Y. Hua, J. Wei, I. A. Sigal, Structured polarized light microscopy for collagen fiber structure and orientation quantification in thick ocular tissues. *J. Biomed. Opt.* **23**, 1–10 (2018).
60. F. Ji, M. Quinn, Y. Hua, P. Y. Lee, I. A. Sigal, 2D or not 2D? Mapping the in-depth inclination of the collagen fibers of the corneoscleral shell. *Exp. Eye Res.* **237**, 109701 (2023).
61. J. Schindelin, I. Arganda-Carreras, E. Frise, V. Kaynig, M. Longair, T. Pietzsch, S. Preibisch, C. Rueden, S. Saalfeld, B. Schmid, J. Y. Tinevez, D. J. White, V. Hartenstein, K. Eliceiri, P. Tomancak, A. Cardona, Fiji: An open-source platform for biological-image analysis. *Nat. Methods* **9**, 676–682 (2012).
62. R. M. S. Sigrist, J. Liau, A. El Kaffas, M. C. Chammas, J. K. Willmann, Ultrasound elastography: Review of techniques and clinical applications. *Theranostics* **7**, 1303–1329 (2017).
63. G. Y. Li, Y. Zheng, Y. X. Jiang, Z. Y. Zhang, Y. P. Cao, Guided wave elastography of layered soft tissues. *Acta Biomater.* **84**, 293–304 (2019).
64. Z. Han, J. Li, M. Singh, S. R. Aglyamov, C. Wu, C. H. Liu, K. V. Larin, Analysis of the effects of curvature and thickness on elastic wave velocity in cornea-like structures by finite element modeling and optical coherence elastography. *Appl. Phys. Lett.* **106**, 233702 (2015).
65. B. F. Kennedy, P. Wijesinghe, D. D. Sampson, The emergence of optical elastography in biomedicine. *Nat. Photonics* **11**, 215–221 (2017).
66. S. Wang, K. V. Larin, Noncontact depth-resolved micro-scale optical coherence elastography of the cornea. *Biomed. Opt. Express* **5**, 3807–3821 (2014).
67. Ł. Ambroziński, S. Song, S. J. Yoon, I. Pelivanov, D. Li, L. Gao, T. T. Shen, R. K. Wang, M. O'Donnell, Acoustic micro-tapping for non-contact 4D imaging of tissue elasticity. *Sci. Rep.* **6**, 38967 (2016).
68. W. Qi, R. Chen, L. Chou, G. Liu, J. Zhang, Q. F. Zhou, Z. Chen, Phase-resolved acoustic radiation force optical coherence elastography. *J. Biomed. Opt.* **17**, 110505 (2012).
69. X. Zhang, T. Osborn, S. Kalra, A noninvasive ultrasound elastography technique for measuring surface waves on the lung. *Ultrasonics* **71**, 183–188 (2016).
70. T. Shiina, N. Nitta, E. Ueno, J. C. Bamber, Real time tissue elasticity imaging using the combined autocorrelation method. *J. Med. Ultrason.* **29**, 119–128 (2002).
71. J. Zhu, L. Qi, Y. Miao, T. Ma, C. Dai, Y. Qu, Y. He, Y. Gao, Q. Zhou, Z. Chen, 3D mapping of elastic modulus using shear wave optical micro-elastography. *Sci. Rep.* **6**, 35499 (2016).
72. R. Righetti, J. Ophir, P. Ktonas, Axial resolution in elastography. *Ultrasound Med. Biol.* **28**, 101–113 (2002).
73. R. Righetti, S. Srinivasan, J. Ophir, Lateral resolution in elastography. *Ultrasound Med. Biol.* **29**, 695–704 (2003).
74. I. Sanchez, R. Martin, F. Ussa, I. Fernandez-Bueno, The parameters of the porcine eyeball. *Graefes Arch. Clin. Exp.* **249**, 475–482 (2011).

Acknowledgments: We thank C. Marks from the Core Center in Nano Imaging (CNI) of USC for guidance in SEM and TEM imaging. Figure 2 and fig. S3 were created by BioRender, under authorization from the University of Southern California. **Funding:** This work was supported by the National Institutes of Health (NIH) under grants R01EY032229, R01EY028662, R01EY030126, R01HL125084, R01EB030024, R01EB030558, and R01EY023966; Unrestricted Grant to the Department of Ophthalmology from Research to Prevent Blindness, New York, NY; and Stein Innovation Award from Research to Prevent Blindness to I.A.S. Research reported in this publication was also supported by the National Eye Institute of the National Institutes of Health under award numbers P30EY029220, P30EY008098, and T32EY017271. The content is solely the responsibility of the authors and does not necessarily represent the official views of the National Institutes of Health. R.L. acknowledged the USC Provost Fellowship and the Alfred E. Mann Innovation in Engineering Post-Doctoral Fellowship. **Author contributions:** Zh.C., I.A.S., and Q.Z. conceived and designed experiments. R.L. and X.Q. developed the UE system. R.L. performed the experiment with imaging phantom, chicken breast, and porcine eyes with UE. R.L. designed and fabricated the ultrasonic transducer for OCE. F.Z., R.L., and W.J. performed the experiment with imaging phantom, chicken breast, and porcine eyes with OCE. Y.H. and S.W. performed the experiment with sheep tendon and porcine eyes with PLM. R.L. performed the SEM and TEM imaging and analysis. R.L., C.G., X.W., Y.Z., Zi.C., and J.Z. contributed to the data analysis. M.S.H., Zh.C., I.A.S., and Q.Z. supervised this study. R.L. and I.A.S. wrote the manuscript. All authors provided critical feedback on the research and the manuscript. **Competing interests:** The authors declare that they have no competing interests. **Data and materials availability:** All data needed to evaluate the conclusions in the paper are present in the paper and/or the Supplementary Materials.

Submitted 15 April 2024
Accepted 5 June 2025
Published 9 July 2025
10.1126/sciadv.adp8631